

The Development Features and Design of a Vibratory Gyroscope with a Metallic Cylindrical Resonator

Valerii CHIKOVANI¹, Serhii HOLOVACH¹*, Hryhorii STROKACH²,
Vadym AVRUTOV²

¹) *National Aviation University*

Kyiv, Ukraine; e-mail: valerii.chikovani@npp.nau.edu.ua

²) *National Technical University of Ukraine "Igor Sikorsky Kyiv Polytechnic Institute"*

Kyiv, Ukraine; e-mails: gr.strokach@gmail.com, v.avrutov@kpi.ua

*Corresponding Author e-mail: golovach.s@meta.ua

This paper presents the results of developing a vibratory gyroscope with a cylindrical resonator made of Elinvar alloy. The vibratory gyroscope operates in three modes. These modes include rate mode, rate-integrating mode, and a new, third, differential mode. The differential mode can simultaneously measure two opposite angular rates, Ω and $-\Omega$. A block diagram of the standing wave control system for each mode is presented. The advantages and disadvantages of each of the modes are analyzed. A triple-mode gyro is proposed. The results of experimental studies and simulation data are also presented.

Keywords: vibratory gyroscope; standing wave; control system; auto-compensation.



Copyright © 2025 The Author(s).
Published by IPPT PAN. This work is licensed under the Creative Commons Attribution License
CC BY 4.0 (<https://creativecommons.org/licenses/by/4.0/>).

1. INTRODUCTION

The Coriolis vibratory gyroscope (CVG) is chronologically the latest gyroscopic technology available on the global market today, although the effect of the sensitivity of elastic waves to inertial rotation was discovered by G.H. BRYAN in 1890 [1]. He considered the uniform rotation of a vibrating ring. Almost a century later, D.D. LYNCH experimentally confirmed this effect for a ring rotating with a variable angular rate [2]. After that, the theoretical [3, 4] and practical development of the vibratory gyroscope began [4, 5]. Today, vibratory gyroscopes are used in various orientation and navigation systems on land [6, 7], on water [8], and in the air and space [9, 10].

A CVG is a sensor whose operation principle is based on detecting changes in the vibration of a resonator under the influence of Coriolis forces [2, 3]. Vibra-

tion in the resonator is generated by exciting it at a specific resonant frequency, resulting in the formation of a standing wave within the resonator. Resonators in vibratory gyroscopes are generally divided into two classes. The first class includes design where the vibration modes are different but have acceptably close resonance frequencies (e.g., beam, tuning fork, double tuning fork). The second class includes resonators with identical vibration modes, represented by two orthogonal modes of a rotationally body (e.g., hemisphere, cylinder, ring), as shown in Fig. 1 [11].

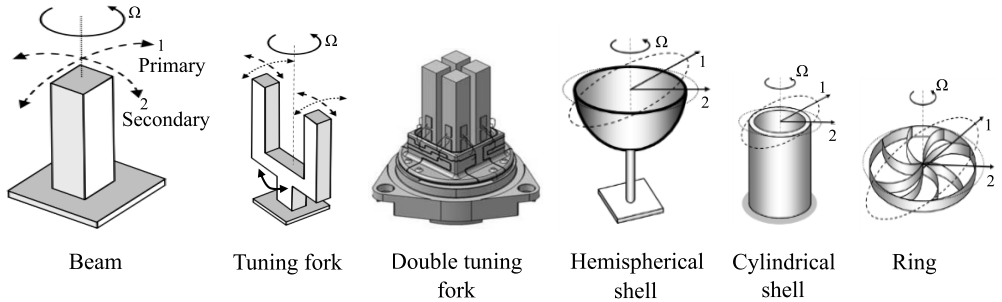


FIG. 1. Examples of structural implementations of the CVG sensing elements of the first and second classes.

Resonators with geometries based on bodies of rotation, i.e., structures with strict axial symmetry such as a hemisphere, cylinder, ring, and similar forms, generally offer higher accuracy. Modern micro-electro-mechanical systems (MEMS) technologies are also advancing the development of rotationally symmetric resonators. In this work, the object of research is a CVG with a metallic cylindrical resonator made of Elinvar alloy. Such a gyroscope can be easily manufactured. It can be produced in factories using standard mechanical equipment and is compatible with mass production methods such as powder metallurgy and additive manufacturing. This approach makes the gyroscope cost-effective, while navigational accuracy is achieved through the stability of the resonator material and the application of modern error correction and auto-compensation methods.

The commonly known modes of CVG operation are the rate mode and the rate-integrating mode (also known as the whole angle mode). In the rate mode, the standing wave is rigidly held in place by negative feedback applied to the drive (excitation) electrode of the primary oscillations, so that the deflection angle is zero, $\theta = 0$. When the angular rate is applied, Coriolis forces arise, and the resulting force is measured by another electrode and compensated for by feedback. This ensures that the primary standing wave maintains its position at $\theta = 0$ under the influence of the angular rate, i.e., it rotates along with the gyroscope at the same angular rate. The feedback signal that compensates for

the Coriolis force is proportional to the angular rate. This mode of operation is the most popular, and it is used in most MEMS and non-MEMS gyroscopes [12–16].

In the rate-integrating mode, or as it is also called the whole angle mode, there is no feedback, and the standing wave rotates under the influence of Coriolis forces relative to the gyroscope, with a delay. This delay coefficient is called the scale factor of the rate-integrating gyroscope, or the Bryan coefficient k . Thus, the rotation angle of the standing wave is proportional to the rotation of the gyroscope in inertial space. This mode is mainly used in high- Q high-precision vibratory gyroscopes based on quartz resonators [7–10].

In this work, a new, third mode of operation – the differential mode – is presented [17, 18]. A key feature of this mode is that the standing wave is positioned between the electrodes so that its oscillation direction does not align with any single electrode. As a result, two measurement channels are formed, allowing the simultaneous detection of angular rates of opposite signs, Ω and $-\Omega$. The differential mode has a unique capability for auto-compensation of both internal and external disturbances [17].

Block diagrams of the standing wave control systems for each operating mode are presented. The advantages and disadvantages of each mode are analyzed. The enhanced auto-compensation capabilities enabled by the differential mode are also presented in this work. Additionally, a control system block diagram is proposed that allows automatic switching between modes, thereby ensuring maximum measurement accuracy under varying motion parameters and environmental conditions. Both experimental results and simulation data are presented.

2. MATHEMATICAL MODEL OF THE TWO-DIMENSIONAL PENDULUM

To ensure a suitable foundation for analyzing all modes of CVG operation, it is necessary to generalize the dynamic equation of oscillations by including the primary components of gyro errors. Manufacturing imperfections and material properties of the resonator determine these errors. Specifically, thickness mismatches in the ring cause two resonant frequencies of the same mode: the maximum frequency ω_1 , and the minimum frequency ω_2 , with corresponding resonator rigidities k_1 and k_2 . Additionally, non-homogeneity in the resonator material leads to two different damping coefficients, which are expressed by two time constants, maximum τ_1 and minimum τ_2 , and their corresponding Q -factors, Q_1 and Q_2 . In addition to these, the angle θ_ω of the minimum (or maximum) frequency axis (or rigidity) and the angle θ_τ of the minimum (or maximum) damping axis relative to the X drive (excitation) electrode are determined, as shown in Fig. 2.

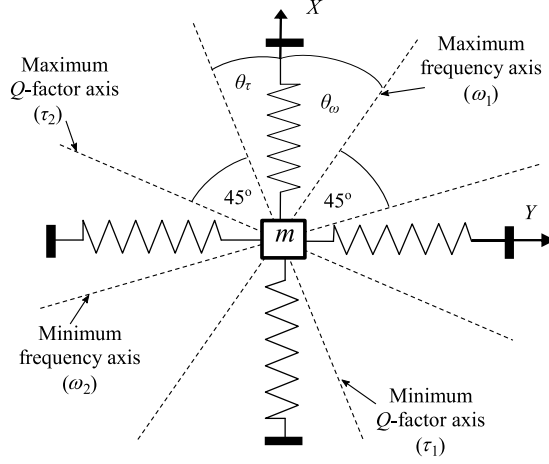


FIG. 2. Two-dimensional pendulum model.

Equations describing oscillations of any resonator are presented as follows:

$$(2.1) \quad \begin{aligned} \ddot{x} - 2k\Omega\dot{y} + d_{xx}\dot{x} + d_{xy}\dot{y} + k_{xx}x + k_{yx}y &= f_x, \\ \ddot{y} + 2k\Omega\dot{x} + d_{yy}\dot{y} + d_{yx}\dot{x} + k_{yy}y + k_{xy}x &= f_y, \end{aligned}$$

where

$$(2.2) \quad \begin{aligned} d_{xx} &= \frac{2}{\tau} + h \cos 2(\theta - \theta_\tau); & d_{yy} &= \frac{2}{\tau} - h \cos 2(\theta - \theta_\tau), \\ d_{yx} = d_{xy} &= h \sin 2(\theta - \theta_\tau); & h &= \Delta \left(\frac{1}{\tau} \right) = \frac{1}{\tau_1} - \frac{1}{\tau_2}, \\ k_{xx} &= \omega_1^2 - \omega\Delta\omega \cos 2(\theta - \theta_\omega); & k_{yy} &= \omega_1^2 + \omega\Delta\omega \cos 2(\theta - \theta_\omega), \\ k_{yx} &= k_{xy} = -\omega\Delta\omega \sin 2(\theta - \theta_\omega), \\ \omega\Delta\omega &= \frac{\omega_1^2 - \omega_2^2}{2}; & \frac{2}{\tau} &= \frac{1}{\tau_1} + \frac{1}{\tau_2}, \end{aligned}$$

where k is the Brian coefficient, d_{xx} and d_{yy} are the damping coefficients of oscillations along the X and Y axes, respectively, d_{xy} is the damping cross-coupling coefficient, k_{xx} and k_{yy} are the normalized resonator rigidities along the X and Y axes, respectively, and k_{xy} is the rigidity cross-coupling coefficient.

These equations have been written for any position of the vibratory standing wave along the circumferential coordinate θ , measured from the X drive electrode.

3. RATE CVG CONTROL SYSTEM BLOCK DIAGRAM AND ITS ADVANTAGES

The most widespread and relatively simple mode of the CVG is the rate mode. This mode enables the measurement of angular rate through a well-defined distribution of electrodes on the sensing element, arranged at specific input and output positions relative to the standing wave's nodes and antinodes (Fig. 3).

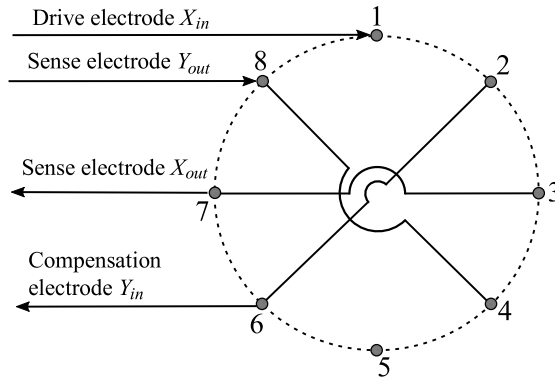


FIG. 3. Electrodes distribution in a ring-type resonator.

This work considers a CVG with a metallic cylindrical resonator made of Elinvar alloy, manufactured by JSC “Elmiz” (Kyiv, Ukraine). Images of the resonator and sensing element are depicted in Fig. 4. The upper thick ring is excited at its resonant frequency on the second mode of ring oscillation using piezo-electrodes. The resonator is mounted on a stem protruding from the base. Plane rectangular piezoelectric electrodes are bonded onto eight spokes. Diametrically opposite electrodes are connected (see Fig. 3), making the sensing element a system with two inputs and two outputs.

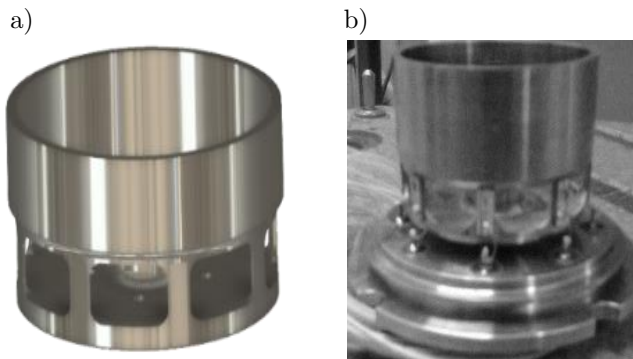


FIG. 4. Metallic cylindrical resonator (a) and sensing element (b).

Let the force f_x , from the first equation of the system (2.1) generate the primary oscillations $x(t)$ of the resonator along the X -axis with amplitude A_0 at frequency ω_x as follows:

$$(3.1) \quad x(t) = A_0 \cos \omega_x t, \quad \omega_x^2 = \omega^2 - \omega \Delta \omega \cos 2\theta_\omega.$$

Then, the equation of oscillations along the Y -axis, assuming $\theta = 0$ (rate mode) and $\Omega \neq 0$ can be written as follows [11]:

$$(3.2) \quad \ddot{y} + \frac{2}{\tau_y} \dot{y} + \omega_y y = f_y + A_0 \omega_x [2k\Omega + \sin 2\theta_\tau] \sin \omega_x t \\ + A_0 \omega \Delta \omega \sin 2\theta_\omega \cos \omega_x t,$$

where

$$\omega_y^2 = \omega^2 + \omega \Delta \omega \cos 2\theta_\omega, \quad \frac{1}{\tau_y} = \frac{1}{\tau} - \frac{1}{2} h \cos 2\theta_\tau.$$

The feedback loop generates the force f_y to compensate for the oscillations along the Y -axis, i.e., to drive the right-hand side of Eq. (3.2) to zero. Thus, the force f_y is given by:

$$(3.3) \quad f_y = -A_0 \omega_x [2k\Omega + h \sin 2\theta_\tau] \sin \omega_x t - A_0 \omega_x \Delta \omega \sin 2\theta_\omega \cos \omega_x t.$$

After amplitude demodulation of (3.3) by the reference signals $\sin \omega_x t$ and $\cos \omega_x t$, the following expressions can be obtained:

$$(3.4) \quad \Omega = \frac{1}{SF} (\text{demod}\{f_y\}|_{\sin \omega_x t} + B); \quad SF = -2k\omega_x A_0; \quad B = \frac{1}{2k} h \sin 2\theta_\tau,$$

where SF is the rate CVG scale factor, B is the rate CVG bias, and $A_0 \omega_x \Delta \omega \sin 2\theta_\omega$ is the quadrature amplitude, representing an error signal caused by the resonator's rigidity mismatch.

Thus, the rate CVG scale factor is proportional to the primary vibration amplitude A_0 . The rate CVG bias is proportional to $h \sin 2\theta_\tau$, where h is proportional to the Q -factor mismatch.

A digital control system block diagram for the rate CVG is presented in Fig. 5. The output signal from the antinode electrode X_{out} , after passing through an analog-to-digital converter (ADC), is divided by signals into two paths. These signals are demodulated by two references signals $\cos \omega_r t$ and $\sin \omega_r t$, to obtain two slow variables C_x and S_x . The S_x component corresponds to the stabilized vibration amplitude A_0 .

While the signal C_x is responsible for tracking the resonant frequency, which may vary during CVG operation. The drive (excitation) signal of the corresponding amplitude is generated at the output of controller PI 2. This signal

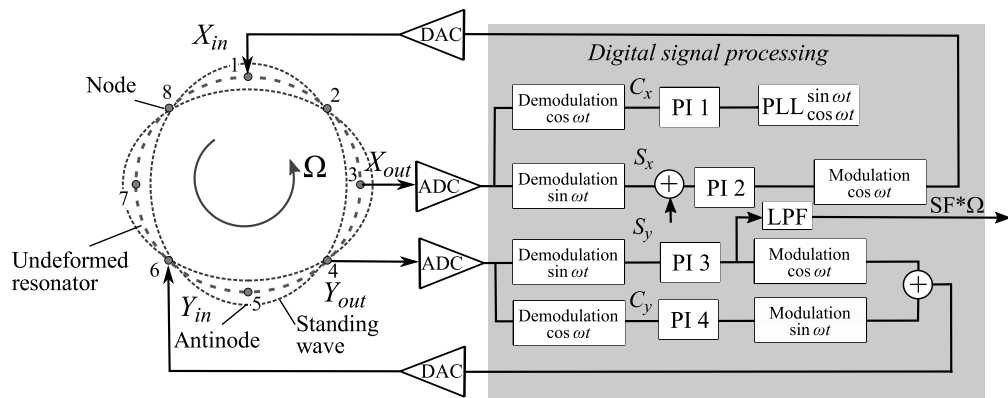


FIG. 5. The rate CVG digital control system block diagram.

is then re-modulated by modulator 2 with the reference signal $\cos\omega_r t$ and sent to the X_{in} electrode after passing through the digital-to-analog converter (DAC).

The most widespread and relatively simple CVG mode is the rate mode. It allows measuring angular rate through a the well-defined distribution of electrodes on the sensing element. These electrodes are positioned relative to the standing wave's nodes and antinodes to serve as inputs and outputs. After the ADC, the signal is split and demodulated by reference signals to obtain two slow variables C_y and S_y . Controllers PI 3 and PI 4 generate corresponding control signals that are re-modulated by the same reference signals, summed, and sent to the compensation electrode Y_{in} to nullify both components, as shown in Fig. 5. The output of controller PI 3 is proportional to the Coriolis force, i.e., the angular rate, while the output of controller PI 4 is proportional to the quadrature amplitude.

Due to Coriolis force compensation in the rate CVG, only the primary, oscillation mode exists in the resonator, and the standing wave is installed with its antinodes positioned close to the X_{in} electrode, rotating together with the resonator at the same angular rate. The trajectory of the antinode point along the rim of the resonator forms a fixed straight line directed along the ring's diameter.

For low-cost MEMS and non-MEMS gyroscopes operating in the rate mode, performing a mass balancing procedure to compensate for Q -factor mismatch is impractical because it is labor-intensive, as opposed to mass balancing aimed at reducing frequency mismatch. As a result, the bias in such gyroscopes can be large relatively.

As will be shown below, both the bias and the scale factor of the vibratory gyroscope using a compensating feedback signal to maintain the standing wave

in a stationary position, depend on its angular position θ . In the rate mode, this angle is $\theta = 0$. However, this angle does not ensure that the bias is close to zero, even for an unbalanced or balanced resonator. Nevertheless, a specific angle θ_0 exists, as shown in Fig. 6b, at which the gyro bias is zero.

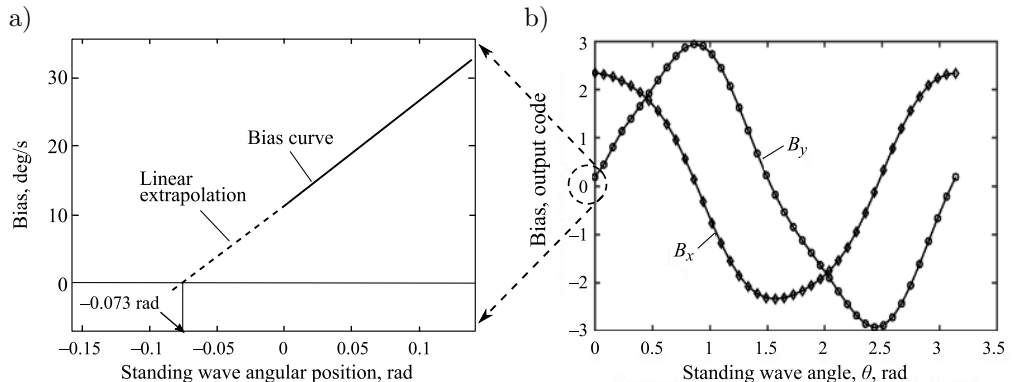


FIG. 6. Extrapolation of the bias curve (a) and X and Y channel biases versus standing wave angular position (b).

Typically, $\theta_\tau \ll 1$ for resonators balanced by frequency mismatch. In this case, taking into account that $\sin x \approx x$, for $x \ll 1$, the angle θ_0 can be determined using linear extrapolation or interpolation. To do this, one needs to first measure the bias at the standing wave position $\theta = 0$, denoted $B(0)$. Then, rotate the standing wave by a small angle $\Delta\theta$ and measure the bias at $\theta = \Delta\theta$, denoted $B(\Delta\theta)$. If $B(\Delta\theta) < 0$, and $B(0) > 0$, linear interpolation is used to find θ_0 where $B(\theta_0) \approx 0$. If both biases have the same sign, linear extrapolation is applied instead.

Figure 6a shows the extrapolation procedure used to determine θ_0 for the unbalanced metallic cylindrical resonator, which gives us the value $\theta_0 \approx -0.073$ rad. Figure 6b shows the periodic dependence of the bias B_y on the standing wave angle θ . This dependence gives us opportunity to apply extrapolation procedure to minimize gyro bias. As can be seen, the bias for an unbalanced resonator at $\theta = 0$ is 11.34 deg/s, but at $\theta_0 = -0.073$ rad it is reduced to 0.0033 deg/s – almost a 3000-fold improvement.

The rate CVG can achieve low-level noise, high sensitivity to angular rate, low sensitivity to manufacturing imperfections of the resonator, and sufficiently high bandwidth for many applications. As an example, Fig. 7 shows a the raw measurement signal a metallic resonator CVG when its sensitive axis is rotated in a horizontal plane passing through four cardinal directions: south, west, north, and east. This curve is usually called the azimuthal characteristic of the gyroscope – the dependence of the gyroscope output signal on the azimuthal orien-

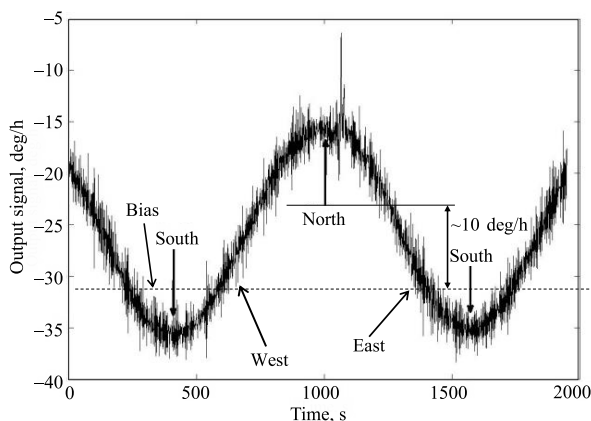


FIG. 7. Metallic resonator rate CVG azimuthal characteristic.

tation of its sensing axis. On average, during the rotation period, the bias value is about 25 deg/s. The maximum corresponds direction to the north direction, the minimum indicates the south direction, and the west and east positions correspond to the points where the bias crosses the average level. The amplitude of the signal is ~ 10 deg/s, which is close to the expected horizontal component of the Earth's angular rate at the laboratory's latitude, which is 9.6 deg/s.

4. A RATE-INTEGRATING CVG CONTROL SYSTEM BLOCK DIAGRAM AND ITS ADVANTAGES

The Coriolis force is not compensated when the vibratory gyroscope operates in the rate-integrating mode (also called whole-angle mode). This leads to the superposition of the primary and secondary waves caused by the Coriolis force during rotation. As a result of this superposition, the standing wave rotates by an angle proportional to the gyroscope angle in inertial space. The proportionality coefficient k between these angles, the standing wave angle and the gyroscope rotation angle, is called the scale factor of the rate-integrating gyroscope, also known as Bryan's coefficient k .

$$(4.1) \quad \theta(t) = -k\alpha(t); \quad \alpha(t) = \int_0^t \Omega(\tau) d\tau,$$

where $\theta(t)$ is the angle of rotation of the standing wave relative to the body of the gyroscope, and $\alpha(t)$ is the angle of rotation of the gyroscope relative to inertial space.

In the absence of rotation, the trajectory of a point on the rim of the resonator (near the antinode) generally moves along the ellipse shown, as shown Fig. 8.

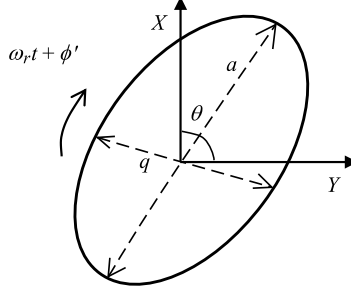


FIG. 8. Trajectory of a point on a resonator rim in a rate-integrating CVG.

The ellipse parameters are determined as follows: a is the vibration amplitude, q is the quadrature amplitude, ω_r is the resonance frequency, ϕ' is the vibration phase, and θ is the angular position of the standing wave relative to the X electrode. These parameters are referred to as the pendulum parameters. They can be calculated from the slow (demodulated) variables C_x , S_x , C_y , and S_y by the following equations [19]:

$$\begin{aligned}
 (4.2) \quad a &= \sqrt{\frac{1}{2} \left(E + \sqrt{E^2 + P^2} \right)}; & q &= \sqrt{\frac{1}{2} \left(E - \sqrt{E^2 + P^2} \right)}; \\
 E &= C_x^2 + S_x^2 + C_y^2 + S_y^2; & P &= 2(C_x S_y - C_y S_x) = 2aq; \\
 \theta &= \frac{1}{2} \operatorname{atan} \frac{C_x C_y + S_x S_y}{S_x^2 + C_x^2 - C_y^2 - S_y^2}; & \phi' &= \frac{1}{2} \operatorname{atan} \frac{2(C_x S_x + C_y S_y)}{C_x^2 - S_x^2 + C_y^2 - S_y^2}.
 \end{aligned}$$

The purpose of the standing wave control system in the rate-integrating mode is to ensure the following conditions:

$$(4.3) \quad P = 0 \rightarrow q = 0, \quad a^2 = E_0 = \text{const}, \quad \phi' = 0,$$

where E_0 is the vibration energy, P is the quadrature error, and a is the vibration amplitude.

The block diagram of the standing wave control system that ensures these conditions is presented in Fig. 9.

Based on the pendulum's parameters, control signals are generated and applied to the X_{in} and Y_{in} electrodes to sustain the oscillation of the standing wave with a constant amplitude at any angular position (θ) of the wave:

$$\begin{aligned}
 (4.4) \quad X_{in} &= D_x E_{pid} \cos \theta \cos(\omega_r t) + D_x P_{pid} \sin \theta \sin(\omega_r t); \\
 Y_{in} &= D_y E_{pid} \sin \theta \cos(\omega_r t) - D_y P_{pid} \cos \theta \sin(\omega_r t),
 \end{aligned}$$

where E_{pid} and P_{pid} are the output signals of the PID controllers responsible for stabilizing the vibration energy squared at the value E_0 and for nullifying the quadrature signal, respectively, and D_x and D_y are the total gain coefficients of the drive channels X and Y .

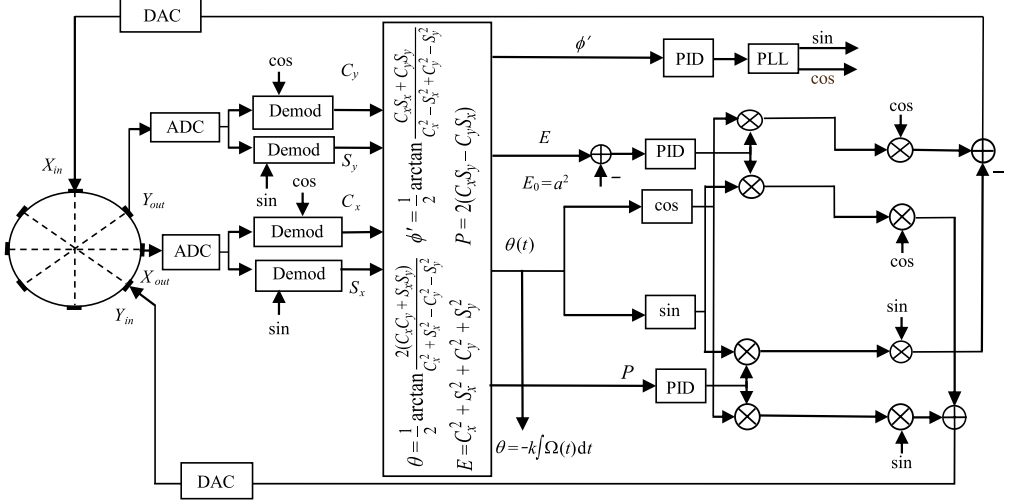


FIG. 9. Rate-Integrating CVG control system block diagram.

When the CVG operates in rate-integrating mode, the resonator errors associated with frequency and Q -factor mismatches lead to insensitivity to small angular rates, known as the dead zone. This effect is analogous to the frequency synchronization of counter-propagating waves in the optical resonator of a laser gyroscope.

The dead zone threshold Ω_{thr} is determined by the following relationship [20]:

$$(4.5) \quad \Omega_{thr} \approx \frac{1}{2k} \left| \Delta \left(\frac{1}{\tau} \right) \right| + \frac{1}{k} \frac{q}{a} |\Delta\omega|; \quad h = \Delta \left(\frac{1}{\tau} \right) = \frac{1}{\tau_1} - \frac{1}{\tau_2} \approx \frac{\Delta Q}{Q} \frac{1}{\tau}.$$

Taking into account Eq. (4.5), the following expression can be written for the scale factor of the gyroscope operating in the rate-integrating mode:

$$(4.6) \quad SF_{int} = \begin{cases} k & \text{for } |\Omega| \gg |\Omega_{thr}|, \\ k \sqrt{1 - \left(\frac{\Omega_{thr}}{\Omega} \right)^2} & \text{for } |\Omega| > |\Omega_{thr}|, \\ 0 & \text{for } |\Omega| \leq |\Omega_{thr}|. \end{cases}$$

For low-cost MEMS and non-MEMS CVGs, the dead zone threshold can reach 10–30 deg/s. Thus, for these gyroscopes, the rate-integrating mode can be

used for measuring large angular rates, up to 7000 deg/s, while maintaining a very stable scale factor k of 35 ppm, even for low-cost gyroscopes [21]. Measurement of small angular rates in the rate-integrating mode can be achieved by using a large virtual angular rate [22].

Figure 10 shows the results of rotation angle measurements with a rate-integrating metallic resonator CVG manufactured by JSC “Elmiz” (Kyiv, Ukraine). The actual constant angular rate was 10 deg/s. To this actual angular rate, a virtual angular rate of $\Omega_{virt} = 803.57$ deg/s was added. Thus, the total angular rate was equal to $\Omega_{act} + \Omega_{virt} = 813.57$ deg/s.

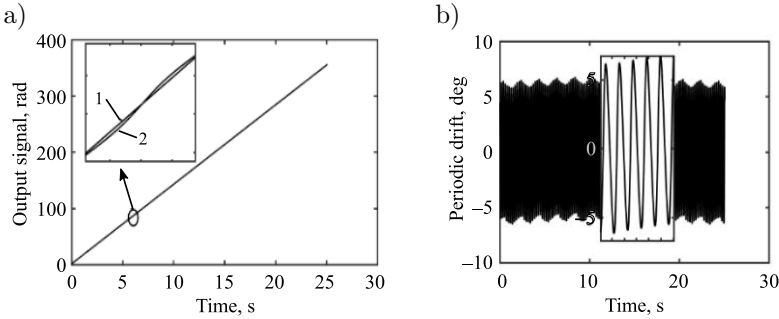


FIG. 10. Rate-integrating CVG with virtual rotation (a) and its periodic drift (b).

Figure 10a shows a straight line 1, which represents the true angle of rotation, while curve 2 depicts the output signal of the rate-integrating gyroscope with a periodic error (drift) primarily caused by the heterogeneity of the resonator. Figure 10b shows this periodic drift extracted using the least squares method. The error period equals half of the standing wave rotation period. The value of this error is determined by the angle θ of the wave orientation and is subject to correction based on the presented model.

Figure 11 shows the result of correcting the periodic drift of the gyroscope according to the proposed model, whose coefficients were obtained by a least squares experimental data approximation presented in Fig. 10a:

$$(4.7) \quad C(\theta) = 0.1063 \sin(2\theta - 0.1947) + 0.006 \sin(4\theta - 0.7848) \\ + 0.0052 \sin(0.2222\theta + 1.2372) - 2.093 \cdot 10^{-10}\theta^2 \\ + 2.5716 \cdot 10^{-6}\theta - 0.0052 \text{ rad.}$$

The root-mean-square correction error is $\Delta\alpha = 0.068$ deg when measuring an angle of about $\alpha \approx 250$ deg. This corresponds to a relative error of $\Delta\alpha/\alpha = 2.7 \cdot 10^{-4} = 0.027\%$.

The advantages of the rate-integrating mode of operation include the ability to measure large and very large angular rates and rotation angles, a wide

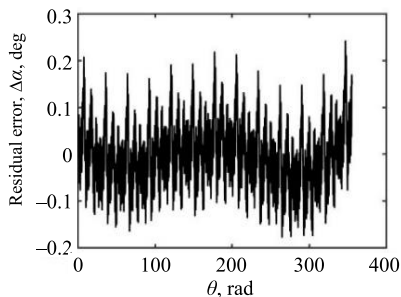


FIG. 11. The residual periodic drift.

bandwidth limited only by information processing capabilities, and a very stable scale factor.

5. THE DIFFERENTIAL CVG CONTROL SYSTEM BLOCK DIAGRAM AND ITS ADVANTAGES

In the differential mode of operation, the standing wave is located between the electrodes, as shown in Fig. 12, i.e., $\theta \neq \pi m/4$, where $m = 0, 1, \dots, 7$. The control system is designed to maintain the standing wave as a predetermined position that does not coincide with any of the electrode locations.

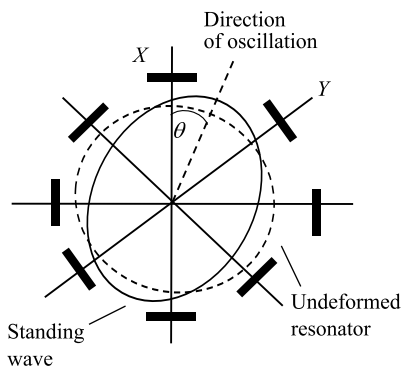


FIG. 12. Standing wave position in a differential CVG.

In this case, as follows from the system of Eq. (2.1), two measurement channels X and Y are formed. These channels measure angular rates of opposite signs Ω and $-\Omega$. The measurement equations in this mode of operation are written as follows [22]:

$$(5.1) \quad \begin{aligned} z_x &= -2k\Omega D_y \sin 2\theta + d_{xx} D_x \cos 2\theta + d_{xy} D_y \sin 2\theta; \\ z_y &= 2k\Omega D_x \cos 2\theta + d_{yy} D_y \sin 2\theta + d_{xy} D_x \cos 2\theta, \end{aligned}$$

where z_x, z_y are the signals of two X and Y measurement channels, D_x , and D_y are the total gain coefficients of the feedback loops, including the transformation coefficients of the X and Y electrodes' deformations into voltages.

It follows from expressions (5.1) that the differential CVG gives information about both Ω and $-\Omega$. The coefficients at Ω represent the scale factors, while the components of the output signals that do not depend on the angular rate represent the biases. Thus, the differential CVG has two scale factors SF_x and SF_y , and two biases B_x and B_y , corresponding to the X and Y channels, respectively. The expressions for these parameters are as follows:

$$(5.2) \quad \begin{aligned} SF_x &= 2kD_y \sin 2\theta; & SF_y &= 2kD_x \cos 2\theta; \\ B_x &= D_x d_{xx} \cos 2\theta + d_{xy} D_y \sin 2\theta; \\ B_y &= D_y d_{yy} \sin 2\theta + d_{xy} D_x \cos 2\theta. \end{aligned}$$

First, it should be noted that both the scale factors and the biases of both channels depend periodically on the standing wave angle θ .

Figure 13 shows the measured scale factors and biases for a metallic cylindrical resonator depending on the wave angle θ . The step size for changing the standing wave angle is $\Delta\theta = 4.5$ deg. The measurements were conducted without turning off the gyroscope [16]. Negative values of the scale factors indicate a change in the sign of the angular rate.

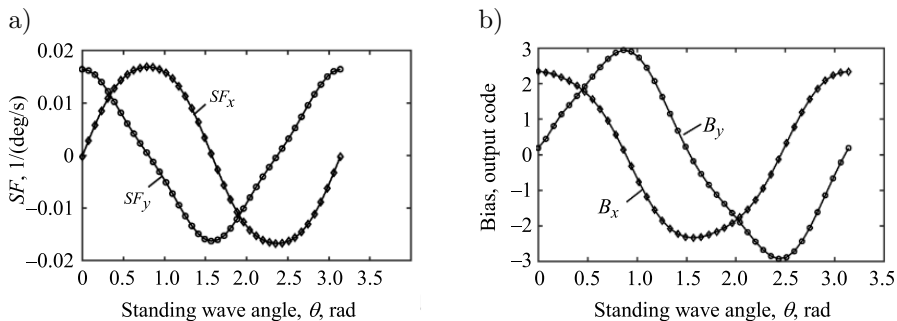


FIG. 13. SF_x, SF_y (a) and B_x, B_y (b) versus standing wave angular position.

The measurements confirm that the biases and scale factors of the two channels are periodic functions, with a period of π rad and phase differences close to $\pi/2$. In addition, the curves intersect, meaning there exists an angle θ_0 at which $B_x(\theta_0) = B_y(\theta_0)$, and an angle θ^* at which $SF_x(\theta^*) = SF_y(\theta^*)$.

In Sec. 3, we presented a method for determining θ_0 , which minimizes $B_y(\theta_0)$ to a value of 0.0033 deg/s ≈ 12 deg/h, using an extrapolation procedure.

In this section, we present a more accurate determination of θ_0 by applying an iterative Newton's zero-search algorithm to the difference $B_x(\theta_0) - B_y(\theta_0)$.

A block diagram of the standing wave control system, which maintains the standing wave in any predetermined position, is shown in Fig. 14.

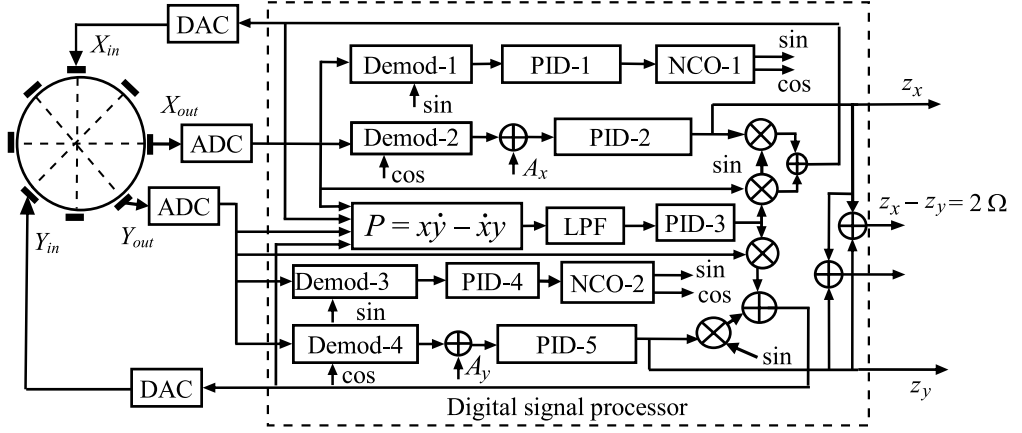


FIG. 14. Differential CVG control system block diagram.

The angular rate signals are generated at the outputs of PID controllers 2 and 5, denoted as z_x and z_y , respectively, as shown in the block diagram in Fig. 14. Their sum $z_s = z_x + z_y$ and difference $z_d = z_y - z_x$ are calculated from these two signals.

Two numerically controlled oscillators, NCO-1 and NCO-2, excite the resonator at the resonant frequencies ω_x and ω_y , respectively, by applying control signals to the X_{in} and Y_{in} electrodes. These signals establish oscillation amplitudes A_x and A_y , which determine the angular position θ of the standing wave relative to the X_{in} electrode according to the expression:

$$(5.3) \quad \theta = \frac{1}{2} \operatorname{atan} \frac{A_y}{A_x}.$$

The quadrature signal P is fed to a low-pass filter (LPF) and then to PID controller PID-3 to minimize this signal to zero. As a result, the resonant frequencies along the X - and Y -axes become equal to each other during the operation of the gyroscope. The behavior of resonant frequencies along the X - and Y -axes in the differential CVG, under the control system presented in Fig. 14, is shown in Fig. 15.

The difference between these output signals doubles the angular rate signal and compensates for the large biases in both channels. Their sum compensates for the angular rate when the standing wave angle is θ^* , where $SF_x(\theta^*) = SF_y(\theta^*)$, and can also be used for real-time estimation of the bias components online.

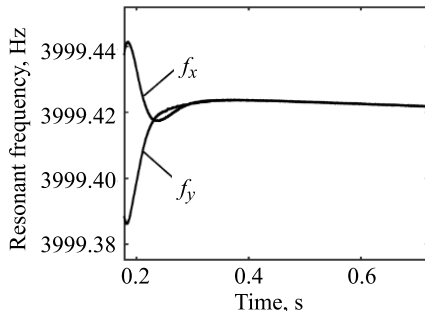


FIG. 15. Frequency mismatch compensation in differential CVG.

5.1. Advantages of differential mode of operation

First, it should be noted that the differential mode auto-compensates for frequency mismatch, i.e., $\Delta\omega = 0$ (Fig. 15). Secondly, at the angle $\theta = \theta^*$, the scale factors of both channels are equal to each other. At this wave angle, the difference z_d and the sum z_s of the X and Y channels can be written as follows [22]:

$$z_d(\theta^*) = z_y(\theta^*) - z_x(\theta^*) = SF_d(\theta^*)\Omega + (d_{yy} - d_{xx}) \frac{D_x D_y}{\sqrt{D_x^2 + D_y^2}}, \quad (5.4)$$

$$SF_d(\theta^*) = 4k \frac{D_x D_y}{\sqrt{D_x^2 + D_y^2}},$$

$$z_s = z_y + z_x = \frac{D_x D_y}{\sqrt{D_x^2 + D_y^2}} (d_{yy} + d_{xx}) + \frac{D_y (D_x + D_y)}{\sqrt{D_x^2 + D_y^2}} d_{xy}. \quad (5.5)$$

As we can see from Eq. (5.5), the sum of the measurements from the two channels compensates for the angular rate and provides real-time information about the bias' components d_{xx} , d_{yy} , and d_{xy} .

Figure 16 presents differential CVG output signals for constant angular rates $\Omega = \pm 40$ deg/s.

Figure 16a shows fairly high biases in the X and Y channels, determined by the parameters d_{xx} and d_{yy} , respectively. Figure 16b shows the near-zero bias of the differential channel $z_d/2 = (Y - X)/2$, which results from the partial mutual compensation of the two channel biases during signal subtraction. The sum signal $z_s/2 = (X + Y)/2$ is independent of the angular rate and is a combination of the bias components from X and Y channels. Therefore, this sum can be used for real-time estimation of the bias components during angular rate measurement.

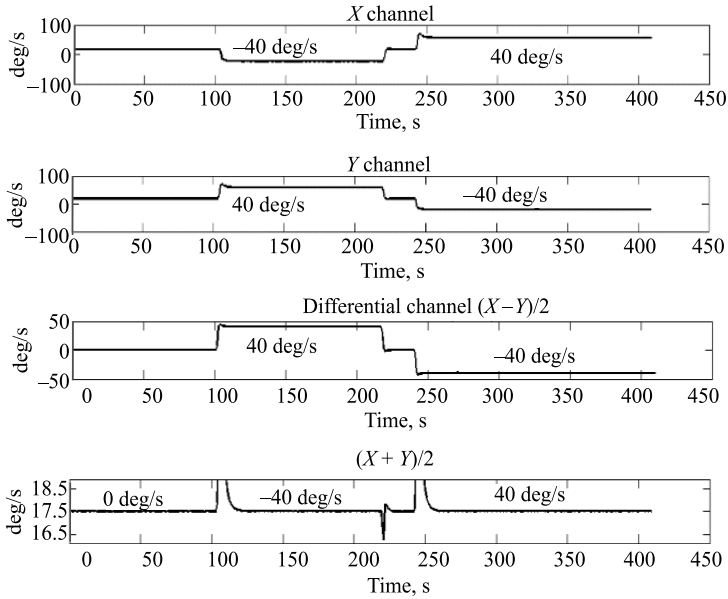


FIG. 16. Differential CVG output signals for constant angular rates $\Omega = \pm 40$ deg/s.

At the wave angle $\theta = \theta^*$, where $SF_x(\theta^*) = SF_y(\theta^*)$, the $z_d/2$ differential channel effectively compensates for external disturbances such as shocks, vibrations, external permanent and variable magnetic fields, and acoustic disturbances at the resonant frequency. In particular, the differential mode is most effective at compensating for magnetic fields and sound disturbances near the resonant frequency.

Figure 17 presents measurement results of a metallic resonator CVG subjected to a permanent magnetic field with intensities ranging from 20 to 480 mT. As we can see from Fig. 17a, the influence of the magnetic field on both the X and Y channels is quite significant, but since their responses are nearly identical, the differential channel shows minimal reaction to the magnetic field.

Figure 17b shows the sensitivities of the channels to a permanent magnetic field. The sensitivity of the X channel to the magnetic field is $4.54 \cdot 10^{-3}$ (deg/s)/mT, the Y channel is $4.2 \cdot 10^{-3}$ (deg/s)/mT, and the differential channel is $1.7 \cdot 10^{-4}$ (deg/s)/mT. The ratio of the minimum sensitivity of the X and Y channels to that of the differential channel can be determined as the coefficient of suppression of the magnetic field by the differential CVG, which is equal to 25.

Figure 18 shows the responses of the three channels X , Y , and the differential one to three acoustic pulses at the resonant frequency. The values of signal spikes in channels X and Y are significant, while in the differential channel, they barely rise above the noise level.

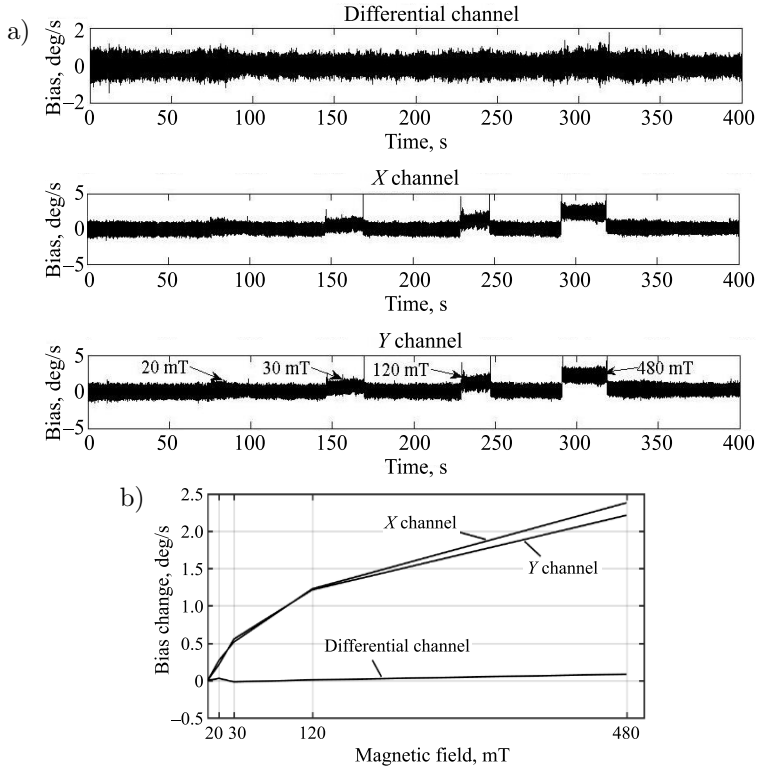


FIG. 17. Differential CVG signal responses to a constant magnetic field (a) and channel sensitivities (b).

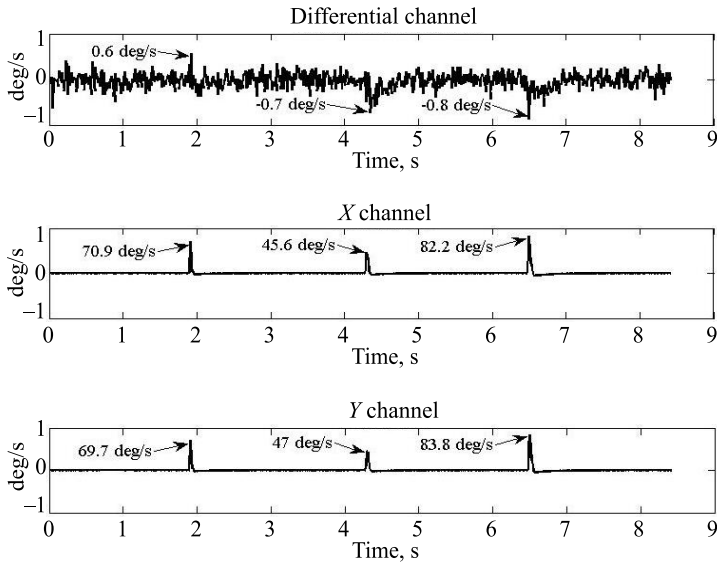


FIG. 18. Differential CVG responses to acoustic impulses at the resonant frequency.

The suppression coefficients of sound pulses by the differential channel are defined as the ratio R of the peak values indicated in Fig. 18. The calculations give the following results: for the first pulse, $R_1 = 69.7/0.6 \approx 116$, for the second pulse, $R_2 = 45.6/0.7 \approx 65$, and for the third pulse, $R_3 = 82.2/0.8 \approx 103$. The lowest of the three is $R_2 = 65$, which corresponds to about 36 dB suppression. Thus, the differential channel suppresses acoustic pulses at the resonant frequency nearly twice as effectively as sound shielding based on metamaterial [24]. Detailed results on shock and vibration suppression measurements are extensively presented in [22].

As shown in Fig. 13b there is a wave angle $\theta = \theta_0$ at which the biases of channels X and Y are equal to each other, i.e., $B_x(\theta_0) = B_y(\theta_0)$, or equivalently $B_x(\theta_0) - B_y(\theta_0) = 0$. To determine the angle θ_0 for differential mode operation, one can use the bias models of the X and Y channels derived from the measurement data presented in Fig. 13b:

$$(5.6) \quad \begin{aligned} B_x(\theta) &= A \cos(2\theta + \theta_x^0), \\ B_y(\theta) &= B \sin(2\theta + \theta_y^0), \end{aligned}$$

where A , B , θ_x^0 , θ_y^0 are the amplitudes and phases of the periodic bias functions for the X and Y channels, respectively.

To determine the angle θ_0 at which $B_x(\theta_0) = B_y(\theta_0)$, two bias measurements at two different standing wave angular positions are required. The simplest choice is to choose $\theta = 0$ and $\theta = \pi/4$. After determining four values of biases $B_x(0)$, $B_y(0)$, $B_x(\pi/4)$, $B_y(\pi/4)$, parameters A , B , θ_x^0 , θ_y^0 can be determined as follows:

$$(5.7) \quad \begin{aligned} \theta_x^0 &= -\text{atan} \frac{B_x(\frac{\pi}{4})}{B_x(0)}; & \theta_y^0 &= \text{atan} \frac{B_y(0)}{B_y(\frac{\pi}{4})}; \\ B &= \frac{B_y(0)}{\sin \theta_y^0}; & A &= \frac{B_x(0)}{\cos \theta_x^0}. \end{aligned}$$

Now, the expression for the angle θ_0 can be obtained by solving the equation $B_x(\theta_0) = B_y(\theta_0)$:

$$(5.8) \quad \theta_0 = \frac{1}{2} \text{atan} \frac{B_x(0) - B_y(0)}{B_y(\pi/4) - B_x(\pi/4)}.$$

Simulation results for low Q -factor resonators ($Q = 21\,000$, Q -factor mismatch $\Delta Q = 1000$, and frequency mismatch $\Delta f = 0.07$ Hz), are presented in Table 1.

TABLE 1. Two-channel biases at different vibration modes.

Bias	Value
$B_y(0)$	$2.594784 \cdot 10^{-4}$
$B_x(0)$	-95.681730
$B_y(\pi/4)$	-86.983730
$B_x(\pi/4)$	$-2.118977 \cdot 10^{-4}$

Calculations using expression (4.8) result in $\theta_0 = 23.863173$ deg.

Figure 19a shows the two-channel biases when the standing wave is positioned at angle θ_0 . The differential gyro output signal $z_d(\theta_0)$, measured when no input angular rate is present (i.e., the bias), is shown in Fig. 19b. The difference $B_{diff}(\theta_0) = B_y(\theta_0) - B_x(\theta_0)$ is the differential gyro bias $B_{diff}(\theta_0) = 2.342945 \cdot 10^{-6}$ (in code units). To convert this bias into deg/s, $B_{diff}(\theta_0)$ should be divided by the scale factor of the differential channel, which is the sum of the X and Y channels' scale factors at a standing wave angle θ_0 . These scale factors are: $SF_x(\theta_0) = 0.019878$ 1/(deg/s), and $SF_y(\theta_0) = 0.018438$ 1/(deg/s). Thus, the scale factor of the differential channel is $SF_d(\theta_0) = SF_x(\theta_0) + SF_y(\theta_0) = 0.038316$ 1/(deg/s) and the bias is:

$$B_{diff}(\theta_0) = 2.342945 \cdot 10^{-6} / 0.038316 = 6.114847 \cdot 10^{-5} \text{ deg/s} \approx 0.22 \text{ deg/h.}$$

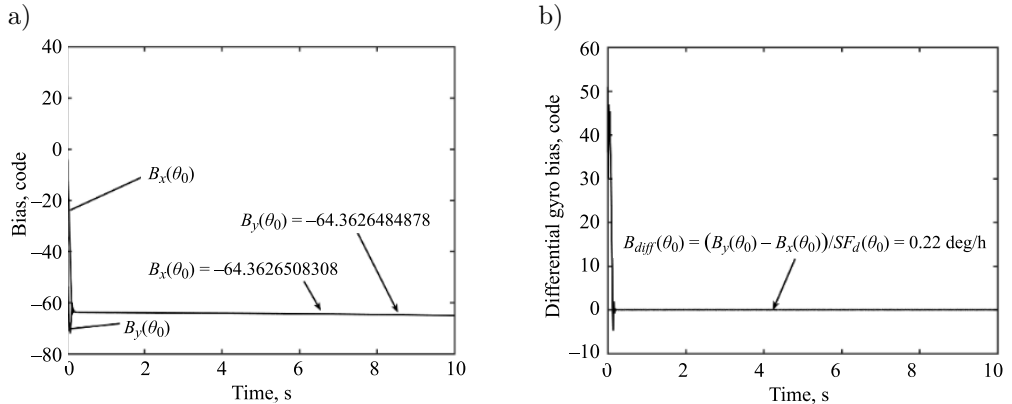


FIG. 19. X and Y channel biases at the standing wave angle θ_0 (a) and the resulting differential gyro bias (b).

This bias value can be obtained when the RMS value of the gyro noise at $\theta = 0$ is about 4 deg/h for an averaging time of 1 s. To reduce this bias value, it is necessary either to lower the gyro noise's RMS value or to increase the averaging time.

By further reducing $B_{diff}(\theta)$, as we discussed above, Newton's method is applied to iteratively find the root of the function $B_{diff}(\theta) = B_x(\theta) - B_y(\theta)$, using the initial value $\theta = \theta_0$ from Eq. (5.8). In our case, because the initial value is sufficiently close to the root, the Newton algorithm for the first iteration:

$$(5.9) \quad \theta_1 = \theta_0 - \left. \frac{B_{diff}(\theta)}{dB_{diff}(\theta)/d\theta} \right|_{\theta=\theta_0},$$

yields the following results:

$$\begin{aligned} \theta_1 &= 23.863173 + 2.342945 \cdot 10^{-6} / 2.586208 \cdot 10^2 = 23.863174 \text{ deg}, \\ B_{diff}(\theta_1) &= B_x(\theta_1) - B_y(\theta_1) = -64.362650 + 64.362650, \\ B_{diff}(\theta_1) &= 5.812240 \cdot 10^{-12} (\text{code}) = 1.516929 \cdot 10^{-10} \text{ deg/s} = 5.461 \cdot 10^{-7} \text{ deg/h}. \end{aligned}$$

Thus, the differential mode of operation can provide a near-zero bias by properly setting the angle of the standing wave. Although each channel bias is large, the bias of the difference channel is close to zero. This solves the problem of bias repeatability when this procedure is used every time the gyro is powered on.

It should be noted that the rate gyro scale factor in this simulation is $SF_y(0) = 0.028456 \text{ 1/(deg/s)}$, which is about 35% less than that of SF_d , because $\sin \theta_0 + \cos \theta_0 > 1$. The same result for the scale factor is also valid for real gyros [22].

Since the bias depends on temperature and, as a rule, drifts slowly, the θ_0 also changes. To maintain the angle θ_0 at the correct value, where $B_x(\theta_0) = B_y(\theta_0)$, it is necessary to conduct tests in a temperature chamber to develop temperature models of the biases B_x and B_y at angles $\theta = 0$ and $\theta = \pi/4$. After this, during the measurement of the angular rate, one needs to change the angle θ_0 by computing it by expression (5.8) using the temperature sensor reading. By doing so, the bias of the differential channel is kept close to zero across the entire operational temperature range. Since the angle theta is calculated as a ratio of two biases (see Eq. (5.8)), which both drift with nearly the same rate, their ratio drifts almost an order of magnitude less than each of them. This results in a more accurate temperature correction of theta compared to the conventional bias temperature correction.

6. TRIPLE-MODE CVG WITH AUTOMATIC SWITCHING BETWEEN MODES

The CVG differs from other modern gyros, such as ring lasers, and fiber optic gyros, in that all three modes of operation, considered here, can be realized in a single CVG, with automatic switching between modes to provide optimal accuracy for various motion parameters and environmental conditions. This triple mode can be realized in both MEMS and non-MEMS CVGs.

The triple-mode CVG control system block diagram, with the capability of auto-switching from one mode to another, is presented in Fig. 20.

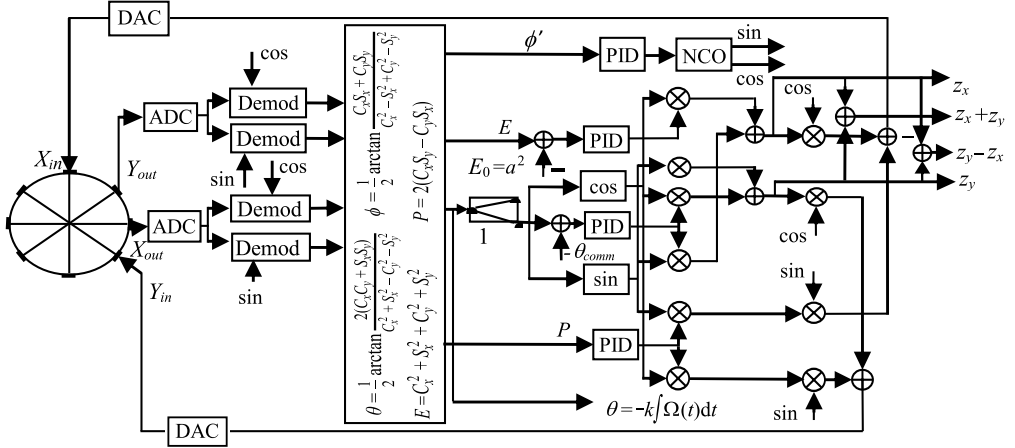


FIG. 20. The triple-mode CVG control system block diagram.

This block diagram is based on the modified rate-integrating control system block diagram presented in Fig. 9. It incorporates switcher 1 to switch from one mode to another. When switcher 1 is set to the position shown in Fig. 20 and the command angle θ_{comm} is equal to zero, $\theta_{comm} = 0$, the system operates in the rate mode. When command angle θ_{comm} is fixed at one of the values from a set of $\theta_{comm} \neq m\pi/4$, the system operates in the differential mode, and when switcher 1 is open (as indicated by the dashed line in Fig. 20), it operates in the rate-integrating mode.

Figure 21 shows the triple-mode gyroscope simulation results with automatic switching from the rate mode to the rate-integrating one, and then the differential mode while measuring a constant angular rate of 100 deg/s.

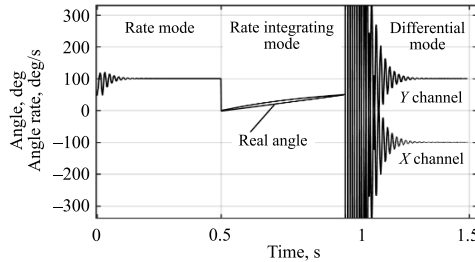


FIG. 21. Triple-mode CVG output signal.

There is no transient process when switching from the rate mode to the rate-integrating mode because the standing wave has no inertia. This means that the

rate-integrating mode theoretically has unlimited bandwidth. In practice, the bandwidth is limited by the information processing. When switching from the rate-integrating to the differential, and then back to the rate modes, transient responses are significant, and the standing wave can become uncontrollable. Similar transients also appear when switching between the rate and differential modes, and vice versa.

To reduce transients during switching, it is necessary to smooth the angle trajectory. For example, Fig. 22 shows the angle trajectory when switching from the rate mode to the differential one. The transient in the gyro output signal under such a trajectory is shown in Fig. 23.

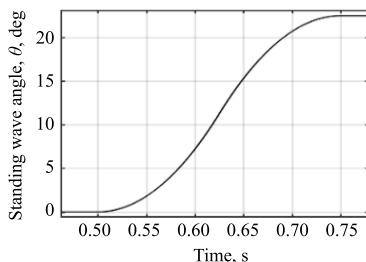


FIG. 22. The smoothed transition trajectory.

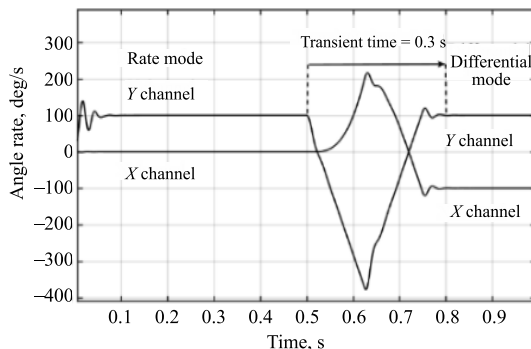


FIG. 23. Transient process under smoothed transition trajectory.

As can be seen, the transient has no oscillatory behavior, the transient time is 0.3 s, and the output signal values in the transient are within the limits of the gyro measurement range. Thus, there is no risk of losing control of the standing wave.

Based on the advantages and disadvantages of the aforementioned modes of operation, a possible variant of switching logic scheme is proposed. The block diagram of this switching logic is depicted in Fig. 24. It aims to provide the maximum possible accuracy for the particular gyroscope, taking into account the vehicle motion parameters and environmental conditions.

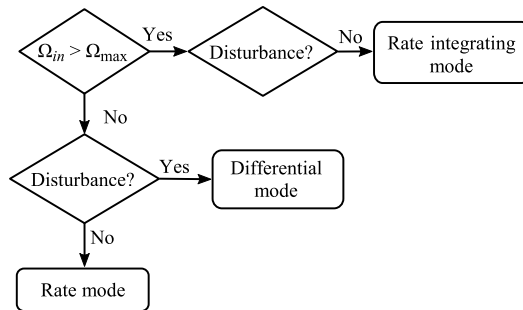


FIG. 24. Example of modes switching logic.

7. CONCLUSIONS

The metallic axisymmetric resonator CVG can reach navigation accuracy due to the stability of the resonator material parameters and error auto-compensation.

The differential mode of operation can be considered the third mode for the CVG and can be integrated along with two other modes (the rate and rate-integrating modes) to form a triple-mode CVG.

The triple-mode CVG can be implemented for both MEMS and non-MEMS gyros.

The differential mode of operation exhibits significantly lower sensitivity to external disturbances compared to the two other modes and can be used under harsh environments, where shocks, vibrations, magnetic fields, and acoustic pulses at the resonant frequency occur.

Implementing a triple-mode CVG provides the gyroscope with enhanced versatility, enabling optimal accuracy under varying motion parameters and environmental conditions, outperforming many other gyroscopic technologies.

DECLARATION OF CONFLICTING INTEREST

The authors declare that there are no known competing financial interests or personal relationships that could have influenced the work reported in this paper.

REFERENCES

1. BRYAN G.H., On the beats in the vibrations of a revolving cylinder or bell, *Proceedings of the Cambridge Philosophical Society*, **7**: 101–114, 1890.
2. LYNCH D.D., Hemispherical resonator gyro, *IEEE Transactions on Aerospace and Electronic Systems*, **7**: 432–433, 1984.

3. GLYNN C.C., On the resonant nonlinear traveling waves in a thin rotating ring, *International Journal of Non-Linear Mechanics*, **17**(5/6): 327–349, 1982, [https://doi.org/10.1016/0020-7462\(82\)90003-8](https://doi.org/10.1016/0020-7462(82)90003-8).
4. ZHURAVLEV V.F., KLIMOV D.M., *Wave Solid-State Gyroscope* [in Russian: *Волновой твердотельный гироскоп*], Nauka, Moscow 1985.
5. SCOTT W.B., Delco makes low-cost gyro prototype, *Aviation Week & Space Technology*, **117**(17): 64–72, 1982.
6. DELHAYE F., HRG by SAFRAN: The game-changing technology, [in:] *Proceedings of 5th IEEE International Symposium on Inertial Sensors and Systems (INERTIAL)*, Lake Como, Italy, 2018, <https://doi.org/10.1109/ISISS.2018.8358163>.
7. BEITIA J., FELL C., OKON I., SWEENEY P., Low cost CVG for high-grade north finders and targeting systems, *2014 DGON Inertial Sensors and Systems (ISS)*, Karlsruhe, Germany, pp. 1–15, 2014, <https://doi.org/10.1109/InertialSensors.2014.7049408>.
8. JEANROY A., BOUVET A., REMILLIEUX G., HRG and marine applications, *Gyroscopy and Navigation*, **5**(2): 67–74, 2014, <https://doi.org/10.1134/S2075108714020047>.
9. DELHAYE F., GIRAULT J.P., SpaceNaute®: HRG technological breakthrough for advanced space launcher inertial reference system, [in:] *Proceedings of 25th Saint Petersburg International Conference on Integrated Navigation Systems (ICINS)*, St. Petersburg, Russia, 2018, <https://doi.org/10.23919/ICINS.2018.8405891>.
10. ROZELLE D.M., The hemispherical resonator gyro: From wineglass to the planets, [in:] *Proceedings of 19th AAS/AIAA Space Flight Mechanics Meeting*, **134**: 1157–1178, 2009.
11. LYNCH D.D., *Coriolis vibratory gyroscope. IEEE standard specification format guide and test procedure for Coriolis vibratory gyros*, IEEE Standard 1431TM, Annex B, pp. 56–66, 2004.
12. TRUSOV A.A., PHILLIPS M.R., BETTADAPURA A., ATIKYAN G., MCCAMMON G.H., PAVELL J.M., CHOI Y.A., SAKAIDA D.K., ROZELLE D.M., MEYER A.D., MHRG: Miniature CVG with beyond navigation grade performance and real time self-calibration, [in:] *Proceedings of 2016 IEEE International Symposium on Inertial Sensors and Systems*, Laguna Beach, CA, USA, 2016, pp. 29–32, <https://doi.org/10.1109/ISISS.2016.7435537>.
13. GREGORY J.A., *Characterization Control and Compensation of MEMS Rate- and Rate-Integrating Gyroscopes*, Ph.D. Dissertation, Michigan University, 2012.
14. CHO J.Y., *High-Performance Micromachined Vibratory Rate- And Rate-Integrating Gyroscopes*, Ph.D. Dissertation, Michigan University, 2012.
15. SU Zh., LIU N., LI Q., FU M., LIU H., FAN J., Research on the signal process of a bell-shaped vibratory angular rate gyro, *Sensors*, **14**(3): 5254–5277, 2014, <https://doi.org/10.3390/s140305254>.
16. CHIKOVANI V., GOLOVACH S., Rate vibratory gyroscopes bias minimization by the standing wave angle installation, [in:] *Proceedings of 2020 IEEE 40th International Conference on Electronics and Nanotechnology (ELNANO)*, Kyiv, Ukraine, pp. 706–709, 2020, <https://doi.org/10.1109/ELNANO50318.2020.9088820>.
17. CHIKOVANI V.V., SUSHCHENKO O.A., TSIRUK H.V., External disturbances rejection by differential single-mass vibratory gyroscope, *Acta Polytechnica Hungarica*, **14**(3): 251–270, 2017, <https://doi.org/10.12700/APH.14.3.2017.3.15>.

18. CHIKOVANI V., SUSHCHENKO O., Self-compensation for disturbances in differential vibratory gyroscope for space navigation, *International Journal of Aerospace Engineering*, **2019**: 5234061, 2019, <https://doi.org/10.1155/2019/5234061>.
19. LYNCH D.D., Vibratory gyro analysis by the method of averaging, [in:] *Proceedings of II Saint Petersburg Conference on Integrated Navigation System. Part I*, May 24–25, 1995, pp. 26–34, 1995.
20. PRIKHODKO I.P., ZOTOV S.A., TRUSOV A.A., SHKEL A.M., Foucault pendulum on a chip: Rate integrating silicon MEMS gyroscope, *Sensors and Actuators A: Physical*, **177**: 67–78, 2012, <https://doi.org/10.1016/j.sna.2012.01.029>.
21. JEANROY A., FEATONBY P., CARON J.M., Low-cost miniature and accurate sensors for tactical applications, [in:] *Proceedings of 10-th Saint Petersburg International Conference on Integrated Navigation Systems, May, 2003*, pp. 286–293, 2003.
22. CHIKOVANI V.V., *Vibratory Gyroscopes Based on Micro-Electro-Mechanical and non-Micro-Electro-Mechanical Systems*, Cambridge Scholars Publishing, 2023.
23. CHIKOVANI V.V., SUSHCHENKO O.A., AZARSKOV V.M., BEZKOROVAINYI Y.M., KOROLOV V.M., KOROLOVA O.V., Errors compensation of ring-type MEMS gyroscopes operating in differential mode, [in:] *Proceedings of 2020 IEEE XVIIth International Conference on the Perspective Technologies and Methods in MEMS Design (MEMSTECH)*, Ukraine, Lviv 22–26 April 2020, pp. 68–71, 2020, <https://doi.org/10.1109/MEMSTECH49584.2020.9109455>.
24. YUNKER W.N., STEVENS C.B., FLOWERS G.T., DEAN R.N., Sound attenuation using microelectromechanical systems fabricated acoustic metamaterials, *Journal of Applied Physics*, **113**(2): 024906 2013, <https://doi.org/10.1063/1.4774021>.

Received October 30, 2024; accepted version March 25, 2025.

Online first June 10, 2025.
